Available online at www.sciencedirect.com
ScienceDirect
Trans. Nonferrous Met. Soc. China 33(2023) 2613−2630
Transactions of Nonferrous Metals Society of China
www.tnmsc.cn

Effects of heat treatment on mechanical properties and degradation behavior of hollow glass microsphere reinforced Mg−15Al−5Zn−1.5Cu composites

Lin LIU[1*], Si-rong YU[1*], Bing-ying WANG[1*], Guang ZHU[2], En-yang LIU[1]

1. School of Materials Science and Engineering, China University of Petroleum (East China), Qingdao 266580, China;
2. State Key Laboratory for Marine Corrosion and Protection,
Luoyang Ship Material Research Institute, Qingdao 266237, China

Received 14 March 2022; accepted 30 September 2022

Abstract: This work focused on enhancing the comprehensive performance of a novel hollow glass microsphere reinforced Mg−15Al−5Zn−1.5Cu composites through heat treatment. Optical microscopy and scanning electron microscopy were employed to characterize the microstructure evolution. Using a combination of compression tests, immersion tests and electrochemical tests, the effects of heat treatment on mechanical properties, and degradation behavior, as well as the influence mechanisms were comprehensively examined. The results demonstrated that variations in the quantity and shape of the $Mg_{17}Al_{12}$ and Al_2CuMg phases were primarily responsible for changes in the mechanical properties and degradation rate of the composites. After solution treatment at 420 °C for 20 h and aging at 200 °C for 24 h, the composites exhibited a more uniform microstructure and distribution of secondary phases, and the segregation and residual stress were also eliminated. This endowed the composites with a desirable overall performance: ultimate compressive strength of 435 MPa, hardness of HB 124, fracture strain of 8.3%, and degradation rate of 151 mg/(cm^2·d) at room temperature, which made them more beneficial to the applications involving degradable downhole tools.

Key words: degradable Mg matrix composites; heat treatment; microstructure; mechanical properties; degradation behavior

1 Introduction

Owing to the excellent features including lightweight, high specific strength and stiffness, easy processing and so on, magnesium (Mg) based alloys or composites have been extensively employed in various engineering fields. Particularly in the unconventional oil and gas exploration field, they have drawn an enormous attention as a novel degradable downhole temporary plugging tool [1−3]. The downhole temporary plugging tools (like fracturing ball, sliding sleeve, etc.) are the essential parts that could effectively isolate each interval to achieve hydraulic fracturing for the reservoir. The plugging tools must be strong enough to bear the intense hydraulic pressure required for the hydraulic fracturing process, after which they need to be eliminated by dissolving themselves to free the way for oil and gas production [4,5]. In order to achieve oil and gas production in time, the degradable plugging tools should possess a high degradation rate in the underground liquid environment. Therefore, it has become an urgent task to simultaneously improve the mechanical properties and degradation rate of the Mg-based materials.

*Lin LIU, Si-rong YU and Bing-ying WANG contributed equally to this work
Corresponding author: Si-rong YU, Tel: +86-18266639928, E-mail: upcyusr@163.com;
Bing-ying WANG, Tel: +86-15063960509, E-mail: tdwby2004@126.com
DOI: 10.1016/S1003-6326(23)66285-5

Alloying is an effective way that has been widely designed to modify the mechanical properties and degradation rate of Mg-based materials. The commonly used elements for alloying includes Al [6,7], Zn [8, 9], Zr [10], Cu [3,11], Ni [1,12], rare earth elements (such as Y [13], and Gd [3,14]) and so on [15]. According to reports, adding high contents of Al and Zn (Al: > 12 wt.%, Zn > 2.5 wt.%) to the degradable Mg alloys can contribute to a greater corrosion rate [16,17]. Cu, Fe and Ni elements usually exist as insoluble particles [6] or cathodic intermetallics (for example, Mg_2Cu, MgAlCu [7], and Mg_2Ni [1,12]) in the Mg alloys. They can dramatically accelerate the galvanic corrosion rate of α-Mg since their potentials are higher than α-Mg matrix. Meanwhile, it is reported that the precipitated intermetallics or insoluble particles have the effects of refining grains or dispersion strengthening, resulting in an enhancement of mechanical properties [1,6,11,12]. In response to the demand for high-strength and rapid-degradation for the downhole tools, our previous research [2,11,18,19] have successfully synthesized a new Mg-based composites by incorporating hollow glass microspheres (HGMs) into degradable Mg−Al−Zn−Cu alloy (denote as MA/HGMs composites). High levels of Al and Zn (15 wt.% Al, 6 wt.% Zn) were added to strengthen the composites while an appropriate amount of Cu (0.3−2 wt.%) was used to accelerate degradation. The HGMs particles with a hollow thin-walled structure could decrease the density of the composites effectively. Meanwhile, it was shown that the addition of HGMs increased the compressive strength and degradation rate significantly. Therefore, the obtained MA/HGMs composites were endowed with necessary mechanical strength and quick degradation in the chloride solution, indicating promise for applications as fracturing tools. However, it should be noted that the matrix alloy of the MA/HGMs composites belongs to the Mg−Al−Zn series, and there is still potential for enhancing the mechanical properties through proper heat treatment, so as to expand its applications in high-pressure or hyper-pressure wells. While the heat treatment can affect the microstructural change and redistribution of alloying elements, which will inevitably influence the degradation behavior of the composites. But this effect is yet not well known. Therefore, to obtain preferable materials for applications involving degradable downhole tools, 4 wt.% HGMs reinforced Mg−15Al−6Zn−1.5Cu composites were prepared, after which the effects of heat treatment (solution treatment and aging treatment) on microstructure, mechanical properties and degradation behavior of the composites were investigated.

2 Experimental

2.1 Composites preparation and heat treatment

The MA/HGMs composites (nominal composition: 4HGMs/Mg−15Al−6Zn−1.5Cu, wt.%) were made from pure Mg, Al, Zn (>99.8%), copper powders (99.9%, 325 mesh), and HGMs (3M Company, average particle size: 20 μm) in an electric resistance furnace under a protective atmosphere of CO_2 and SF_6 (100:3, volume ratio). A stir casting method was employed to achieve the mixing procedure of the melt. Firstly, the Mg, Al and Zn ingots together with the steel crucible were put into the resistance furnace to completely melt at 750 °C, subsequently the copper powders wrapped in Al foil were added and kept for 15 min. Next, the melt was mechanically stirred for 1 min to homogenize the alloying elements. To weaken the excessive interface reaction between the molten Mg and HGMs, the HGMs were introduced to the melt after the temperature was reduced to 590 °C. Prior to this operation, the HGMs were preheated in the baking oven for 2 h, and then added to the vortex of the semi-solid melt formed by a cross stirrer. Finally, the melt was rapidly heated to 720 °C and poured into a graphite mold (preheated to 200 °C). The practical component of the as-cast composites was detected using a plasma-atomic emission spectrometer, and the results are as follows: Al 16.22, Zn 5.65, Si 1.21, Cu 1.58, and Mg balance (wt.%).

The as-cast composites was subjected to different heat treatments including solution treatment and aging treatment. The solution treatment was carried out at 420 °C, and the solution time was 5, 10, 15, 20, and 25 h, respectively (the samples were denoted as S5, S10, S15, S20, and S25). Aimming to retain the microstructure, the samples were immediately quenched in water after solution treatment. Afterward, the solution-treated composites (420 °C,

20 h) were subjected to aging treatment at 200 °C, with an aging time of 4 to 32 h (the samples were denoted as SA4, SA8, and SA12).

2.2 Microstructural characterization

The microstructure of the samples was examined using an optical microscope (Zeiss Axio Scope A1) and a scanning electron microscopy (SEM, JEOL JSM−7200F) equipped with the energy-dispersive X-ray spectroscope (EDS). Before observing the microstructure , the specimens were ground successively with abrasive paper of 600−2000 grades, polished using 0.5 μ diamond paste and etched with the oxalic acid solution (3 wt.%). According to the ASTM E112—2013 standard, the average grain size of the as-cast and heat-treated samples was determined using the linear intercept method by the Pro Imaging software. The phase compositions of the composites before and after heat treatment were identified by X-ray diffraction (XRD, PANalytical) using Cu K_α radiation (λ=0.154 nm).

2.3 Mechanical properties test

The compression test was performed on the cylindrical specimens with the dimensions of d10 mm × 20 mm by a Shimadzu CMT−5105 material test machine. At ambient temperature, the compression speed was set as 1.2 mm/min, and the final results were determined by the average from three samples. The hardness of the composites was evaluated using a Brinell hardness testing machine (KB-3000E, Germany) with a 5 mm ball according to the ASTM E10—2018 test method. The applied load was 2450 N and corresponding dwell time was 30 s. For each specimen, the average result from ten testing points was used as the final hardness.

2.4 Immersion tests

Hydrogen evolution and mass loss tests were employed to evaluate the degradation rate of the composites at ambient temperature. Considering the downhole liquid contains a certain concentration of KCl [20] and the Cl^- is the active ingredient that actually causes the composites to degrade, 3 wt.% KCl solution was served as the corrosive medium. According to the ASTM G31—72, the ratio of solution volume and specimen surface area was 20 mL/cm^2. Before the immersion tests, the specimens with the dimensions of d25 mm × 25 mm were polished through 2000-grade abrasive paper, washed with acetone and ethanol, dried in warm air, and weighed. Then the specimens were put into the KCl solution, located on the plastic support in a beaker. The specimens were continuously immersed for 24 h, and the hydrogen evolution volume was recorded in real-time every 30 min during immersion. The method of the hydrogen evolution volume measurement could be referred to Ref. [11]. After immersion, the corroded specimens were ultrasonically cleaned in a mixed solution of 150 g/L CrO_3 and 10 g/L $AgNO_3$ for 3 min to remove the corrosion products, then were rinsed with distilled water, dried and weighed again.

2.5 Electrochemical tests

Electrochemical tests were performed on an electrochemical workstation (CS310H, Corrtest Instrument, China) in 3 wt.% KCl solution at ambient temperature. A three-electrode cell was used, containing a saturated calomel electrode (SCE) as reference electrode, a platinum plate as the counter electrode, and the specimen encapsulated in epoxy resin with 1 cm^2 exposed surface as the working electrode. Prior to the electrochemical tests, the specimens were immersed in the electrolyte and the open circuit potential (OCP) was monitored to achieve a steady state. Electrochemical impedance spectroscopy (EIS) tests were performed with 5 mV perturbation amplitude within the frequency range from 10^5 to 10^{-2} Hz and the EIS data were fitted using the ZSimpWin software. The potentiodynamic polarization tests were carried out with a scanning rate of 0.333 mV/s in the range of −0.5 V to 0.5 V in relation to the OCP. Three repetitions of each test are required to ensure reproducibility.

3 Results and discussion

3.1 Microstructure

Figure 1 shows the optical micrographs of the as-cast and solution-treated MA/HGM composites. It can be observed from Fig. 1(a) that the as-cast composites possessed equiaxed crystal or rosette crystal structures, with an average grain size of (24±5) μm. The precipitates took the forms of strip and fishbone, and the majority were arranged along the α-Mg grain boundaries in a continuous network.

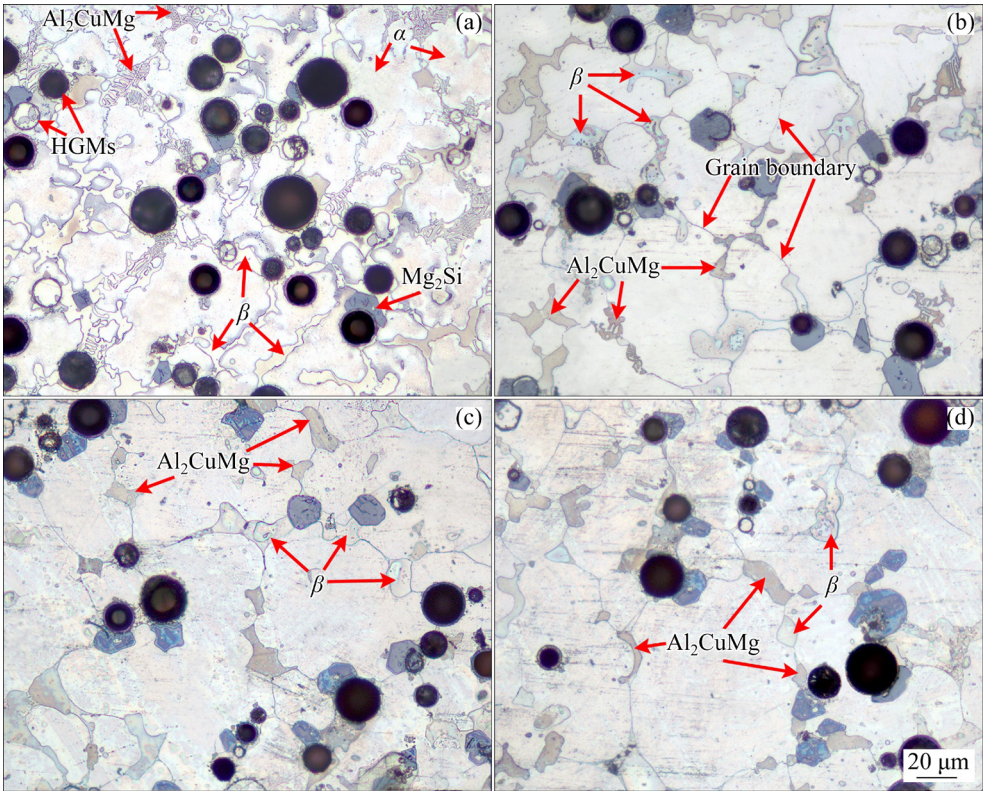

Fig. 1 Optical images of as-cast (a) and solution-treated MA/HGMs composites at 420 °C (b, c, d): (b) 10 h; (c) 20 h; (d) 25 h

The HGMs particles were uniformly distributed in the matrix of the composites. A few polygonal compounds, which were verified as Mg_2Si phase in our previous studies [18,19], distributed around the HGMs particles, which were proven to be the result of interface interactions between the molten magnesium and the HGMs wall. The detailed analyses for the as-cast microstructure of the MA/HGM composites have been reported in previous studies [11,18], the strip-like and fishbone-like precipitates were identified as β-$Mg_{17}Al_{12}$ phase and Al_2CuMg+$Mg_{17}Al_{12}$ eutectic phase, respectively.

After solution treatment, it was seen that the grain of the composites still maintained the equiaxed crystal characteristic similar to that of the as-cast structure, as shown in Figs. 1(b−d), but the grains apparently became coarser with increasing solution time. After solution treatment at 420 °C for 10, 20, and 25 h, the average grain sizes of the composites were about (31±4), (37±3), and (48±3) μm, which increased by 1.3, 1.5 and 2 times respectively compared with the as-cast composites. Furthermore, as the solution time increased, the sharp corners of the polygonal Mg_2Si phase were gradually passivated and the shape tended to be round. The strip-like phase gradually narrowed and its quantity significantly reduced, as well as the fishbone-like phase disappeared. The morphology of the precipitates at the grain boundaries transformed from a continuous network to separate blocks. Additionally, a few isolated residual precipitates were found within the α-Mg grains.

The detailed changes of phase compositions after solution treatment could be further characterized by the XRD and SEM. Figure 2 displays the XRD patterns of the as-cast and solution-treated composites. The composites were all discovered to contain α-Mg, β-$Mg_{17}Al_{12}$, τ-$Mg_{32}(Al,Zn)_{49}$, S-Al_2CuMg, MgO, and Mg_2Si phases both before and after solution treatment. As reported previously, MgO and Mg_2Si were the interface reaction products between the molten magnesium and the HGMs wall [18]. Besides the $Mg_{17}Al_{12}$ and Al_2CuMg phases, a small amount of $Mg_{32}(Al,Zn)_{49}$ phase was also detected, which was previously confirmed to be homogeneously dispersed within the β phase [18,19]. After solution treatment, the diffraction peaks of β and τ phases weakened obviously with increasing time, while

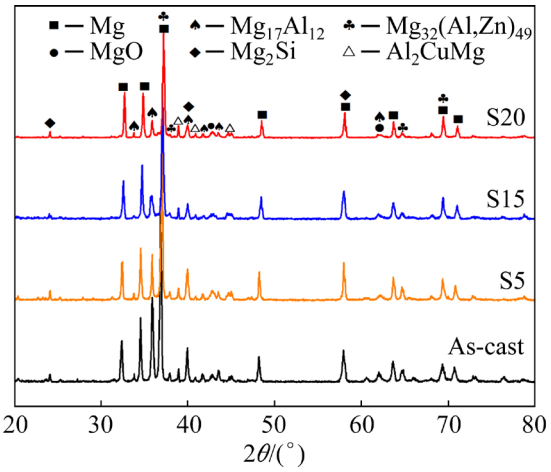

Fig. 2 XRD patterns of as-cast and solution-treated composites

there was no obvious change in the other phases, indicating that $Mg_{17}Al_{12}$ and $Mg_{32}(Al,Zn)_{49}$ phases were partially dissolved into the α-Mg matrix. This is consistent with the results of metallographic observation. In addition, the diffraction peaks for α-Mg detected in solution-treated composites had shifted to the right compared to the as-cast composites. This further demonstrates that the solution treatment made a significant amount of Al atoms dissolved into the Mg lattices, causing the diffraction angle (2θ) of the α-Mg to increase due to the smaller atomic radius of Al (1.43 Å) than that of Mg (1.60 Å).

To further investigate the evolution of the secondary phases during solution treatment, Figs. 3(a−d) present the SEM images of the as-cast

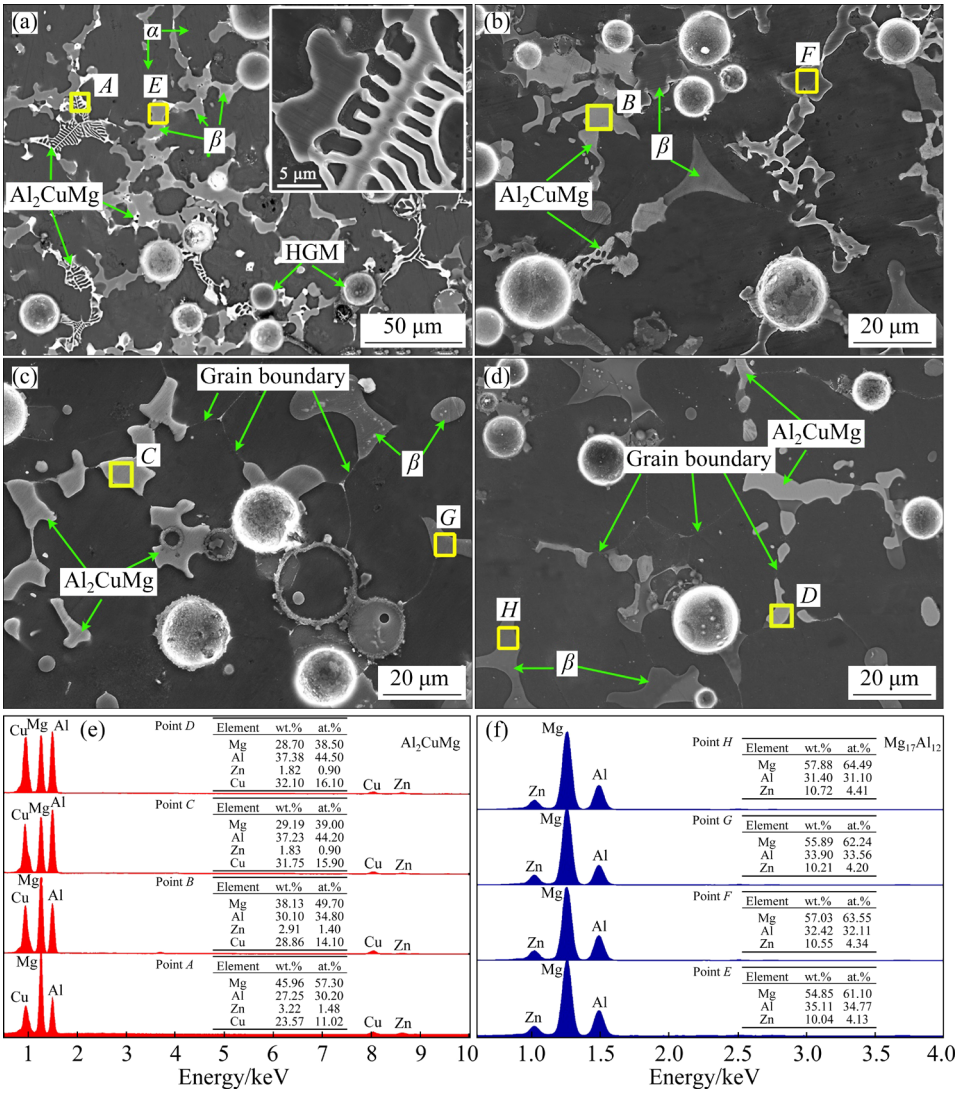

Fig. 3 SEM images of as-cast and solution-treated MA/HGMs composites: (a) As-cast; (b) Solution-treated at 420 °C for 10 h; (c) Solution-treated at 420 °C for 20 h; (d) Solution-treated at 420 °C for 25 h; (e) EDS results of selected area in (a−d); (f) EDS analyses of β phase under different thermal conditions

and solution treated-composites. As shown in Fig. 3(a), the black, gray, and bright phases were α-Mg, β-$Mg_{17}Al_{12}$, and S-Al_2CuMg phases, respectively. The partially magnified image of Fig. 3(a) depicts the fishbone-like precipitate that consists of a central long rod and several parallel fine rods with 1 μm in width and 2−6 μm in length, exhibiting a eutectic feature. Combined with XRD findings, it was identified as Al_2CuMg+$Mg_{17}Al_{12}$ eutectic compound by EDS analysis (Fig. 3(e)). Meanwhile, some bright block or strip-shaped Al_2CuMg phases presented at the edge of the β phase. The formation of the Al_2CuMg phase with different structures had been described in our previous research [11]. After solution treatment at 420 °C for 10 h (Fig. 3(b)), the eutectic S phase underwent a significant change. Although it still remained its eutectic characteristic, the spacing for the fine rods of the eutectic phases grew broader and reduced in quantity. EDS results showed that the atomic ratios of Al and Cu in the eutectic S phase increased, this was likely attributed to the dissolution of the $Mg_{17}Al_{12}$ phase in the eutectic S+β phase. Therefore, it was reasonable to deduce that the dissolution of the $Mg_{17}Al_{12}$ phase caused the "branch" of the eutectic S phase to merge gradually during the solution treatment. With the prolonging of solution time, the fishbone-like eutectic Al_2CuMg phase gradually transformed into blocks, as shown in Figs. 3(b, c). And the atomic ratios of Al and Cu in the Al_2CuMg phase increased to varying degrees (Fig. 3(e)). Simultaneously, it was seen that the block or strip-shaped Al_2CuMg phase at the edge of the β phase became irregular isolate block shape due to the dissolution of the β phase, which was distributed at grain boundaries or in the α-Mg grains. Figure 3(f) shows the component change of the β phase during the solution treatment. There were similar element compositions of the primeval β phase and the residual β phase after solution treatment. This indicates that the β phase together with the $Mg_{32}(Al,Zn)_{49}$ phase dispersed in it and simultaneously dissolved into the α-Mg matrix, which can also be confirmed by the XRD results.

Figure 4 shows the variations of Al, Zn and Cu contents in α-Mg with the solution time. For the as-cast composites, the Al, Zn and Cu contents in the α-Mg were 6.90, 1.14 and 0.24 wt.%. It is well known that Cu has extremely low solid solubility in Mg. There was insufficient time for the Cu atoms to diffuse to the grain boundary during the non-equilibrium solidification, thereby leaving a certain amount of (approximately 0.24 wt.%) Cu in the α-Mg matrix. After solution treatment, there was no obvious change in Cu contents of α-Mg compared with the cast composites. This further confirmed that the Cu atom of Al_2CuMg eutectic did not diffuse into α-Mg, indicating that the Al_2CuMg phase could not be dissolved during the solution treatment. Conversely, Al and Zn contents in α-Mg increased significantly with the increasing solution time. When the solution time increased from 5 to 20 h, the contents of Al and Zn increased to 10.50 and 3.31 wt.%, respectively, suggesting that a large amount of β and τ phases were dissolved to the α-Mg. As the solution time extended to 25 h, the contents of Al and Zn in the α-Mg were barely changed compared to the composites solution treated for 20 h. Therefore, it can be inferred that the solute atoms (Al and Zn) had adequately dissolved in α-Mg after 20 h of solution treatment. Meanwhile, due to the high content of Al (16.22 wt.%, the limited solid solubility of Al in Mg is about 12.7 wt.%) in the composites matrix, some blocky β phases still remained at the grain boundaries after solution treatment, especially at the triple intersections of grains. It should be noted that although extending the solution treatment time could increase the super-saturation of the quenched composites, which is beneficial to the subsequent aging, excessive solution treatment time would lead to the overgrowth of the grains (this can be seen from the optical images). This would have a negative effect on the mechanical properties of the composites.

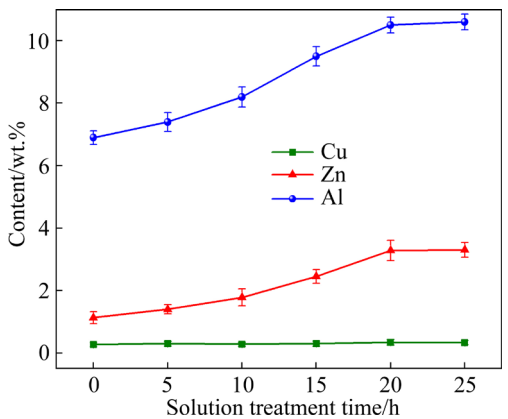

Fig. 4 Variation of Al, Zn and Cu contents in α-Mg with solution time

Figure 5 displays the SEM images of the solution treated composites (420 °C, 20 h) aged at 200 °C for different time. From Fig. 5(a), some fine precipitates appeared near the grain boundaries and the residual second phases after the composites suffered from aging treatment for 8 h. During the aging process, the grain boundary was the preferential location for the formation of the precipitates [10], while the residual second phases could act as nucleation sites of the precipitates. The partially enlarged image (Fig. 5(b)) shows that the formed precipitates have an irregular granular morphology. EDS analysis indicated that the chemical components of the precipitate were similar to the original β phase of as-cast composites. In addition, from the XRD patterns in Fig. 6, the diffraction intensity of $Mg_{17}Al_{12}$ and $Mg_{32}(Al,Zn)_{49}$ peaks enhanced with the increasing aging time. Consequently, it can be determined that the precipitate generated during aging was $Mg_{17}Al_{12}$+$Mg_{32}(Al,Zn)_{49}$. Extended aging time resulted in significantly denser precipitates that eventually grew into larger blocks. When the aging time was further prolonged to 32 h, the increasing precipitates and residual second phases connected together at the grain boundaries, forming a continuous network structure, as displayed in Fig. 5(d). In contrast, due to the lower aging temperature, the blocky Al_2CuMg phase did not experience significant change over the whole aging process.

3.2 Mechanical properties

In order to evaluate the effects of solution and aging treatment on the mechanical properties of the composites, the compressive properties and Brinell hardness of the composites were tested, and the obtained results are shown in Fig. 7. It can be seen that the ultimate compressive strength (UCS) of the composites slightly changed during solution treatment, which increased from 335 to 352 MPa as the solution time extended from 0 to 20 h. However, solution treatment had a noticeable influence on the ductility and hardness. With longer solution time, the ductility significantly increased while the hardness sharply decreased. Compared with the as-cast composites, the composites had a very large compressive fracture strain (9.3%) and a very low Brinell hardness (HB 88) when solution treated at 420 ℃ for 20 h. In addition, the results showed that when the solution time further increased to 25 h, the UCS had slight reduction (decreased to 340 MPa). These variations were closely related to the changes in the microstructure during solution treatment.

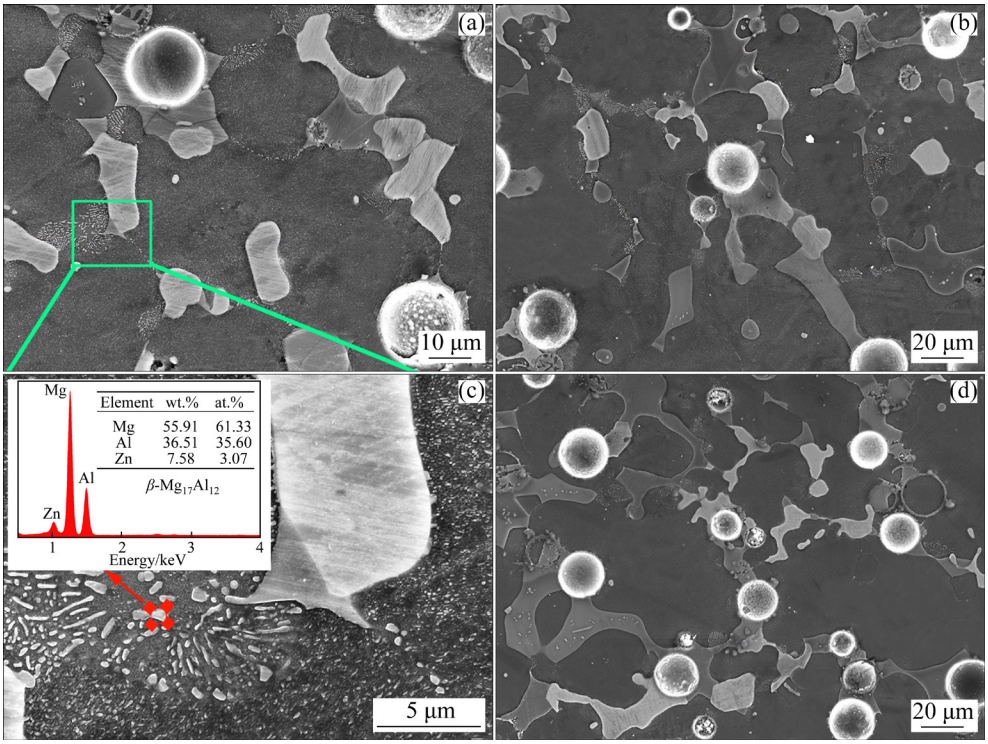

Fig. 5 Microstructure evolution of solution-treated composites (420 °C, 20 h) during aging at 200 °C for different time: (a, b) 8 h; (c) 16 h; (d) 32 h

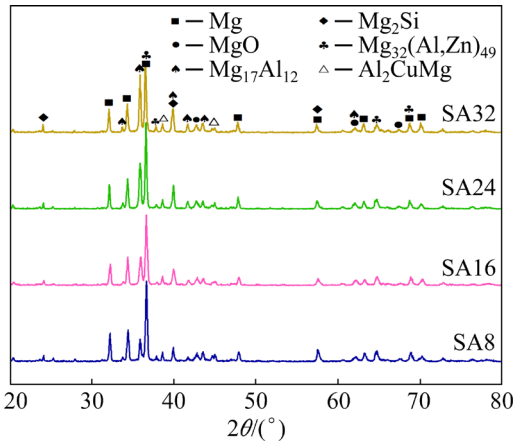

Fig. 6 XRD patterns of composites after aging treatment for different time

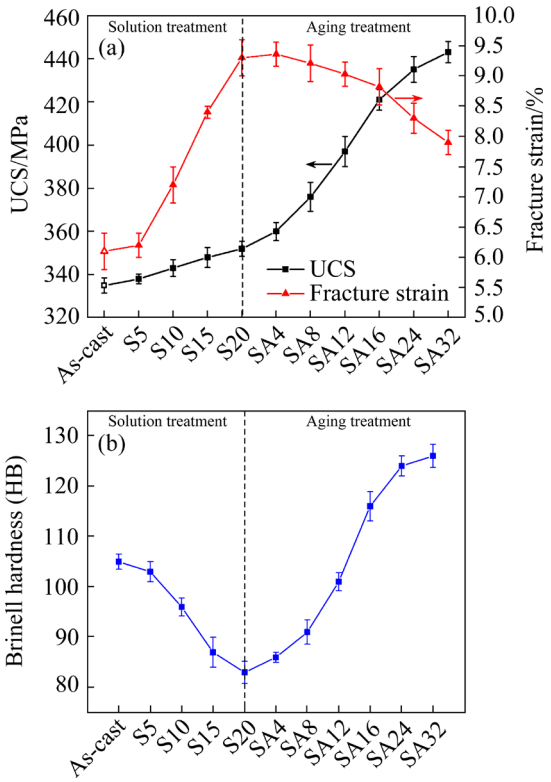

Fig. 7 Variation of mechanical properties of composites during heat treatment: (a) Compressive properties; (b) Brinell hardness

After solution treatment, the β and τ phases dissolved into the α-Mg matrix, causing an enhancement of solid solution strengthening effect of Al and Zn. Nevertheless, since the β phase was an effective strengthening phase, fewer of it would result in a weakened second phase strengthening effect. In addition, the grain growth also negatively affected the strength. Hence, the combined effects of the enhanced solution strengthening and the diminished second phase strengthening led to the minor change in the UCS. Even while the amount of the β phase was no longer reduced as the solution duration extended from 20 to 25 h, the spacing of the residual β phase distributed at the grain boundaries did increase due to the overgrowth of the grains, thereby causing the compressive property to deteriorate. Moreover, the decline in hardness during solution treatment could be ascribed to the reduction in the hard β phase and the excessive dispersion of the residual β phase as a result of grain growth, which caused the dislocation motion to not be hindered effectively during indentation.

Our previous investigation has revealed that the coarse eutectic Al_2CuMg compound was easily broken to generate cracks when the composites bear compressive loads, and these cracks tended to propagate along the grain boundaries due to the precipitation of network brittle β phase there [11]. Hence, the fracture mode of the as-cast MA/HGMs composites was intergranular brittle fracture, this also can be proven by the compressive fractured surface in Fig. 8(a). Combined with the EDS mapping images (Fig. 8(b)), it can be seen that there were a great quantity of fractured second phases on the fracture surface, and some secondary cracks (marked by arrows) existed near the Al_2CuMg compound. Moreover, some cracks were observed around the HGMs particles. This was attributed to the residual stress generated around the HGMs during the solidification for the different thermal expansion coefficients between the HGMs and Mg alloy matrix, causing the cracks to occur under the compressive stress. Meanwhile, the accumulation of local strain would result in the stress concentration at the edge angle of the polygonal Mg_2Si, which can also lead to the initiation of cracks during deformation. The above factors were the reasons for the poor ductility of the as-cast composites.

Figure 8(c) displays the fracture morphology of the solution-treated composites, it was flatter than that of the as-cast composites, and hardly any secondary cracks were noted around the second phases and the HGMs particles. This could be because the coarse eutectic Al_2CuMg compound was changed into the block, and the residual stress around HGMs particles was eliminated after the solution treatment. In addition, the solution treatment smoothed the sharp corners of the Mg_2Si

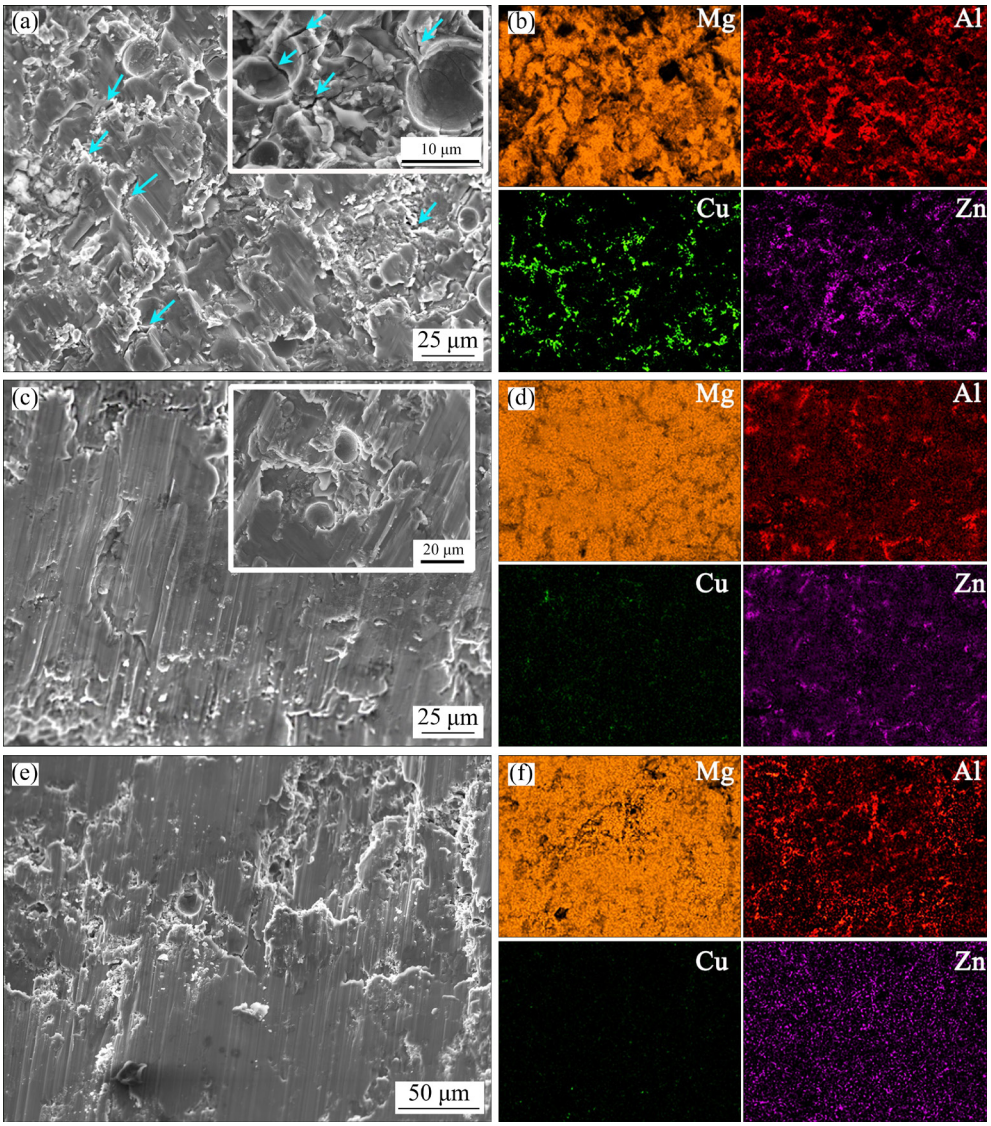

Fig. 8 SEM images of compressive fractured surface of composites and corresponding EDS mapping images: (a, b) As-cast composites; (c, d) S20; (e, f) SA, 24 h

particles, which reduced the stress concentration during deformation. All of these modifications reduced the probability of crack initiation during the compression deformation, thereby improving the ductility. As shown in Fig. 7, the UCS and hardness of the composites were improved after aging treatment, initially rapidly from the start to 24 h, and then slowly over aging time, exhibiting typical age strengthening feature. According to the results of SEM and XRD (Figs. 5 and 6), the fine dispersed β phase gradually precipitated during the aging, which was an effective strengthening phase. In addition, the EDS analyses of the fracture surface (Fig. 8(e)) indicated that the fractured second phase on the fracture surface was mainly β phase, while the Al_2CuMg compound was barely observed, which meant that the uniformly distributed block Al_2CuMg phase might play an inhibition effect on the dislocation motion and crack growth. Therefore, the UCS and hardness were improved greatly. However, the precipitation of the brittle β phase made the fracture of the composites tend to brittle fracture, and the ductility was thereby decreased with the aging time. But compared with the solution treatment, the ductility variation was relatively slight during aging, and this was because the precipitated β phase was more uniformly distributed in the matrix after the aging treatment.

3.3 Degradation behavior

3.3.1 Immersion behavior

The degradation behavior of the as-cast and

heat-treated composites was investigated by immersing in 3 wt.% KCl solution at room temperature for 24 h. The calculated degradation rates are recorded in Fig. 9(a). It is clear that both the solution and aging treatment had significant effects on the mass loss rates of the composites. The mass loss rate of the as-cast composites was 119 mg/(cm^2·d) but it increased to 129 mg/(cm^2·d) after solution treatment for 5 h. When the solution time ranged from 5 to 20 h, the mass loss rate rapidly decreased with the increasing solution time, but it stopped to decrease as long as the solution time exceeded was more than 20 h. As for the aging treatment, the mass loss rate of the composites increased significantly as the time rose. After aging treatment for 24 h, the mass loss rate reached the maximum of 151 mg/(cm^2·d) that was 1.3 times larger than that of the as-cast composites. However, when the aging time was extended to 32 h, the mass loss rate exhibited a tendency to decline. Generally, the aging treatment had a beneficial effect on accelerating the degradation of the composites whereas the solution treatment slowed it. Figures 9(b, c) present the hydrogen evolution rate variations of the composites during immersion. At the initial stage, the hydrogen evolution rates of all the composites tended to increase over time. This was because the corroded area increased with increasing immersion time until the original surface was completely corroded [18]. For the as-cast composites, the hydrogen evolution rate first decreased, following the initial phase, then remained relatively steady. But for the solution-treated composites, only the increase and stable stages were visible, with almost no reduction stages. Figure 9(b) shows that the hydrogen evolution rate of the as-cast composites was 3.6 mL/(cm·h) (at the stabilization stage), then it increased to 4.5 mL/(cm·h) after solution treatment for 5 h. Then it decreased with increasing solution time, the average hydrogen evolution rates of the composites with solution treatment for 10, 15, 20, and 25 h were 3.1, 2.1, 1.4, and 1.4 mL/(cm·h), respectively. Figure 9(c) reveals that the hydrogen evolution rates of the aging-treated composites were significantly accelerated as the aging time increased. When the aging time was extended to 32 h, the hydrogen evolution rate of the composites again exhibited a three-stage characteristic, i.e., first increasing quickly, then declining, and finally

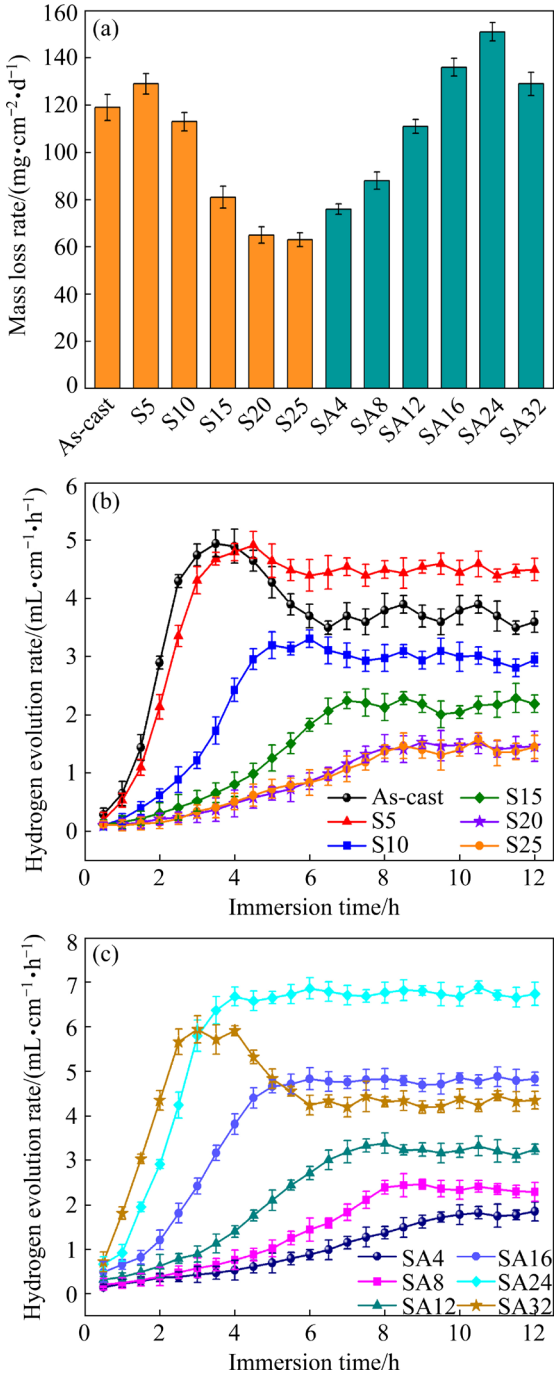

Fig. 9 (a) Mass loss rates of composites after immersion in 3 wt.% KCl solution for 24 h; (b, c) Hydrogen evolution rates of composites during immersion in 3 wt.% KCl solution for 12 h

remaining steady. The results of hydrogen evolution tests were consistent with that of the mass loss tests.

3.3.2 Corrosion morphology

The changes in the degradation behaviors during heat treatment were closely related to the evolution for the microstructure of the composites. It is generally known that the galvanic corrosion

caused by the cathodic second phase is response for the degradation (corrosion) of Mg-based materials. Previous investigations reported that both $Mg_{17}Al_{12}$ and Al_2CuMg compounds possessed more positive potential than the α-Mg matrix, and their amount and distribution could exert significant influence on the corrosion behaviors of the composites [11]. On the one hand, they can act as cathodes to combine with α-Mg to form micro-battery couples, which accelerates the galvanic corrosion of the α-Mg matrix. On the other hand, if the cathode phases form a net-like structure along the grain boundary, they will behave as a corrosion barrier to inhibit the corrosion of the composites [7,21]. Figure 10 exhibits the corrosion morphologies of the composites after immersion in 3 wt.% KCl solution for different time and removal of the corrosion products. It can be seen that both the as-cast and heat-treated composites showed a similar corrosion mode: the corrosion was initiated in pitting corrosion and subsequently propagated gradually. Figures 10(a, d, e) present the corrosion morphologies of as-cast, S20, and SA24 composites after immersion for 1 h, respectively. It showed that the pitting corrosion preferentially occurred on the α-Mg matrix around the β phase, *S* phase and HGM particles, as well as on the α-Mg embedded in the *S* eutectic. Evidently, the corrosion adjacent to the β phase and *S* phase was based on the micro-galvanic mechanism. While the corrosion surrounding the HGM particles could be attributed to the fact that the interface between HGM and Mg matrix was an unstable structure in thermodynamics, making them favorable places for corrosion attack, thus they preferentially suffered from pitting corrosion [11,18]. Meanwhile, some corrosion pits also appeared on the interior of α-Mg grains of the as-cast composites (Fig. 10(a)), this might arise from the inhomogeneous distribution of alloying elements in the as-cast structure. With the increase of immersion time, the amount of the corrosion pit increased and the corrosion would propagate around the preferentially formed corrosion pits, resulting in enlargement of the corroded area. Thus, the hydrogen evolution rate increased with the extended immersion time until the pit corrosion transformed into overall corrosion, as shown in Figs. 9(b, c). For the as-cast composites, as it contained more cathodic phases (Fig. 3), a large amount of micro-galvanic couples immediately formed and the corrosion rapidly propagated once the composites came into contact with KCl solution. As a result, the hydrogen evolution rate accelerated with time. For the solution-treated composites, β phase content decreased with the increase of solution time, so the hydrogen evolution rate increased slowly, and it showed a longer time for achieving overall corrosion. Likewise, the longer the aging time, the more the precipitated β phase, so that the increase of the hydrogen evolution rate was faster at the beginning of immersion, as shown in Fig. 9(c).

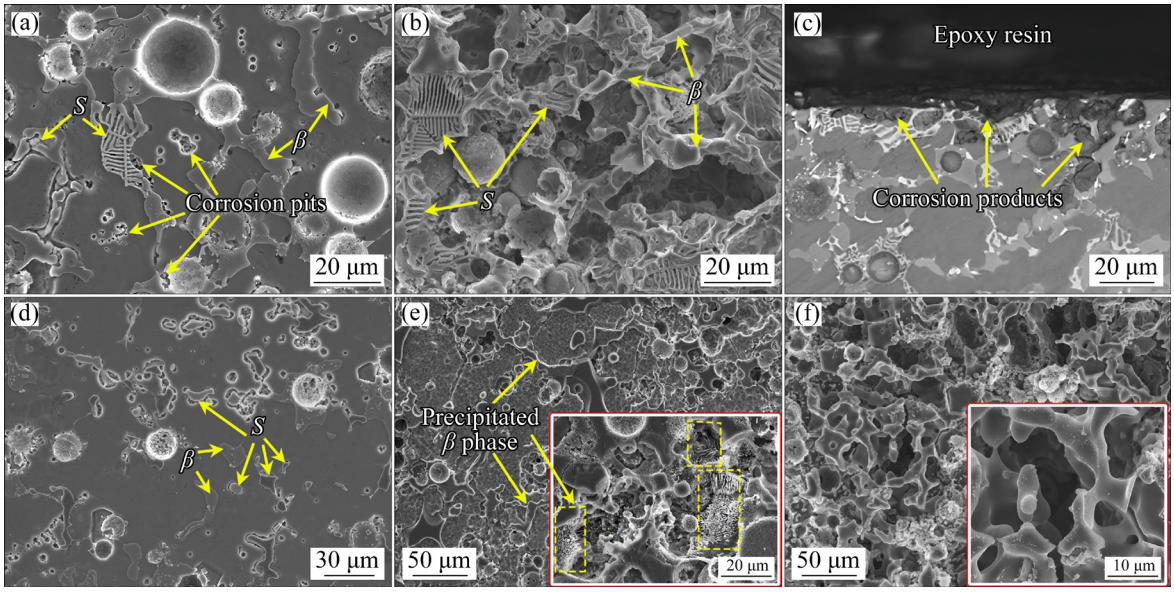

Fig. 10 SEM micrographs of composites after immersion in 3 wt.% KCl solution for different time: (a) As-cast, 1 h; (b) As-cast, 4 h; (c) Cross-section micrograph, as-cast, 4 h; (d) S20, 1 h; (e) SA24, 1 h; (f) SA32, 4 h

As introduced in the above section, β-$Mg_{17}Al_{12}$ phase and the coarse eutectic Al_2CuMg in the as-cast composites compound would connect together to form a net-like structure at the grain boundary (Fig. 3(a)). These net-like cathodic phases made the corrosion difficult to propagate from one grain to another, causing the corrosion pits to propagate vertically along with them. Thus, some deep corrosion holes were formed, as shown in Figs. 10(b, c). Moreover, Fig. 10(b) clearly indicates that these net-like cathodic phases remained on the surface to form a continuous skeleton after the α-Mg grains were corroded. From the cross-section morphology (Fig. 10(c)), the partial corrosion products ($Mg(OH)_2$) would embed in these net-like skeletons to form a cover layer. Despite the fact that the corrosion products layer was porous, it to some extent could still prevent chloride ions from entering, thereby strengthening the passivation property of the corrosion products layer [22]. The existence of the net-like cathodic phases played a certain inhibitory effect on further corrosion. As a result, once the surface of the as-cast composites was completely corroded, the hydrogen evolution rate exhibited an obvious reduction stage due to the coverage of the thickening corrosion products layer, as illustrated in Fig. 9(b). Some cathodic phases would peel off along with the corrosion products when the corrosion spread deeper inside the composites because of the local discontinuity of the cathodic phases and the breakdown of their surrounding α-Mg. A dynamic equilibrium would eventually be reached in the generation, accumulation, and exfoliation of the corrosion products layer, resulting in a relatively stable hydrogen evolution rate.

After solution treatment for 5 h, a few β phase began to dissolve into the α-Mg matrix and the size of the eutectic Al_2CuMg compound became smaller, causing the disconnection of the cathodic network structure made up of them and a reduction in the corrosion barrier effect. As a consequence, the mass loss rate of S5 composites was higher than that of the as-cast composites immersed for a long time. Meanwhile, the reduction in the volume fraction of cathodic phases (β phase and Al_2CuMg phase) during solution treatment also resulted in a decrease in the amount of micro-galvanic couples in the composites. When the solution treatment time exceeded 5 h, the detrimental effect (reducing the galvanic corrosion) caused by the decrease of the β phase began to get more significant and slowed the rate of degradation. Therefore, the degradation rate dramatically reduced as solution time extended from 5 to 20 h. When the solution time was more than 20 h, the volume fraction of the cathodic phase remained relatively stable, the hydrogen evolution rate curve of the S25 composites almost coincided with that of the S20 composites, and the mass loss rates were no significant difference between the two. Figure 5 displays that the shape and amount of Al_2CuMg compounds did not change during the aging treatment, so the amount and distribution of precipitated β phase were undoubtedly the major factors that affected the corrosion behaviors of the aged composites. According to the results of immersion experiments, the rates of degradation accelerated with the aging time. It was apparent that the longer aging time resulted in greater amounts of precipitated β phase, which promoted the galvanic corrosion of the matrix. As described in Fig. 10, SA24 composites showed more serious corrosion than the as-cast and solution-treated composites after immersion for 1 h, with the corrosion nearly covering the whole surface. This was largely because the distribution of the aging-precipitated β phase was more dispersive in the composites, causing lots of micro-galvanic couples to form on the surface once exposed in the KCl solution. Additionally, from the enlarged image in Fig. 10(c), some large exfoliation pits appeared obviously and granular precipitates were observed in the bottom of the pits (marked by the yellow dotted box), indicating that the isolated cathodic phases and the corrosion product began to peel off while the surrounding α-Mg grains were corroded. This meant that due to the more uniform and dispersed distribution of the cathodic phases (blocky *S* phase and aging-precipitated β phase), the corrosion products could timely exfoliate on the corrode surface rather than covering the surface during degradation. This led to a more active dynamic equilibrium. However, when the aging time extended to 32 h, a significant amount of precipitated β phase re-formed a continuous net-like skeleton (Fig. 10(f)), which would be beneficial for the accumulation of the corrosion product on the composites surface and thereby inhibit the invasion of chloride ions, reducing the degradation rate of the composites.

3.3.3 Electrochemical corrosion behavior

In order to further clarify the effect of heat treatment on the degradation behaviors of the composites, the potentiodynamic polarization curves of several representative composites were investigated after immersion in 3 wt.% KCl solution for different times. As shown in Fig. 11, the similar polarization curves of all the composites suggest that their electrochemical corrosion behavior is similar. The curves demonstrated that the as-cast and heat-treated composites were able to continually degrade in KCl solution since there was no evident passive area. Figure 11(a) shows the potentiodynamic polarization curves of the composites in the initial immersion stage (after immersion for 1 h). The cathodic and anodic branches of the polarization curves can be seen to have moved downward following the solution treatment, indicating a reduction in both the cathode hydrogen evolution and the anode dissolution, whereas after the aging treatment, their change tendencies were the opposite. Table 1 provides the values of the Tafel extrapolation-derived corrosion potential (φ_{corr}) and corrosion current density (J_{corr}). It can be seen solution treatment shifted the corrosion potential of the composites towards the more negative direction and aging treatment shifted that towards the more noble direction. The J_{corr} values of as-cast, S5, S20, SA24, SA32 composites were 3.48, 3.05, 1.08, 3.19, and 3.63 mA/cm^2, respectively. It can be observed explicitly that the J_{corr} values became lower after solution treatment and became higher after aging treatment.

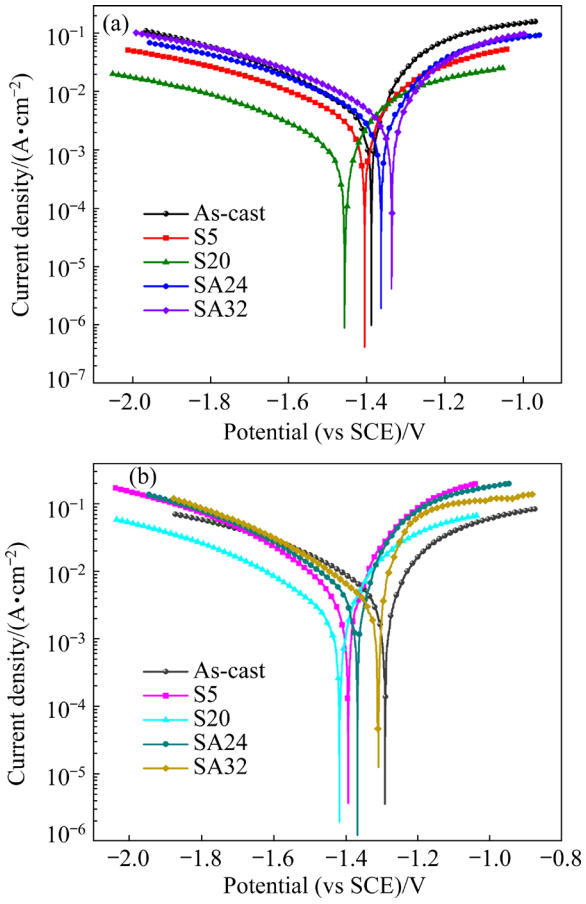

Fig. 11 Potentiodynamic polarization curves of composites after immersion in 3 wt.% KCl solution for different time: (a) 1 h; (b) 5 h (for as-cast, S5, SA24 and SA32) and 8 h (for S20)

Table 1 Fitting results of polarization curves in Fig. 11

Corrosion stage	Sample	φ_{corr} (vs SCE)/V	J_{corr}/(mA·cm^{-2})
Local corrosion	As−cast	−1.388	3.48
	S5	−1.405	3.05
	S20	−1.457	1.08
	SA24	−1.363	3.19
	SA32	−1.355	3.63
Overall corrosion	As−cast	−1.300	4.51
	S5	−1.393	5.12
	S20	−1.436	.2.21
	SA24	−1.360	6.42
	SA32	−1.310	5.75

The microstructure evolution during the heat treatment could be responsible for these results. As mentioned before, the volume fraction of the β phase was significantly reduced by solution treatment. The decrease of the β phase caused a negative shift in φ_{corr} because the potential of the phase was higher than that of the α-Mg matrix. Additionally, this decline led to a reduction in the total area of micro-galvanic corrosion and a corresponding decline in J_{corr}. In contrast, the φ_{corr} values would be increased owing to the precipitation of the β phase during aging treatment Since the distribution of precipitated β phase was more uniform on the composites surface after aging, the potentials of the SA24 and SA32 exhibited a larger extent of the increase than that of the as-cast composites. Moreover, the J_{corr} rose with increasing aging time due to the formation of more micro-galvanic couples. Figure 11(b) shows the potentiodynamic polarization curves of the composites in the overall corrosion stage (after 5 h

of immersion for as-cast, S5, SA24, SA32 composites and 8 h of immersion for S20 composites). The φ_{corr} values of S5, S20, and SA24 composites were nearly unchanged compared to the initial stage, while they exhibited a large increase for the as-cast and SA32 composites, as shown in Table 1. This was evidence that a thicker corrosion product layer formed on the surface of the as-cast and SA32 composites after long-term immersion, which increased the corrosion potential of the composites. Meanwhile, this thick corrosion product layer hindered the migration of ions from the electrolyte to the corroded surface, the J_{corr} values of the as-cast and SA32 composites were thus lower than both S5 and SA24 composites. Another evident result was that the order of J_{corr} values was different in the initial immersion stage and overall corrosion stage. The former stage followed the arrangement of S20 < S5 < as-cast < SA24 < SA32, and the latter followed the arrangement of S20 < as-cast < S5 < SA32 < SA24, which was considerably in line with the results of hydrogen evolution tests.

Figures 12(a−c) present the EIS Nyquist plots of the composites obtained under different thermal conditions immersed in 3 wt.% KCl solution for different time. The Nyquist plots of all composites had the same loop structure at different time, including one high-frequency capacitance loop, one medium-frequency capacitance loop and one low-frequency inductive loop. The electric double layer and the corrosion product layer on the electrode surface were reported to be the causes of the high- and medium-frequency capacitance loops, respectively [23,24]. And the inductive loop was relevant to the desorption behavior of the corrosion intermediates (such as Mg^{+}_{ads}, $Mg(OH)^{+}_{ads}$ and H_{ads}) [25]. With the purpose of clearly interpreting the EIS plots, an equivalent circuit (EC) was established using ZSimpWin analysis software, as shown in Fig. 12(d). The detailed fitting parameters are listed in Table 2, and the low chi-square values indicated great fitting accuracy. In the EC, R_{ct} and Q_{ct} were the charge transfer resistance and interface capacitance of the electrode/solution electric double layer, respectively, corresponding to the high-frequency capacitance loop. R_f and Q_f represented the resistance and equivalent capacitance caused by

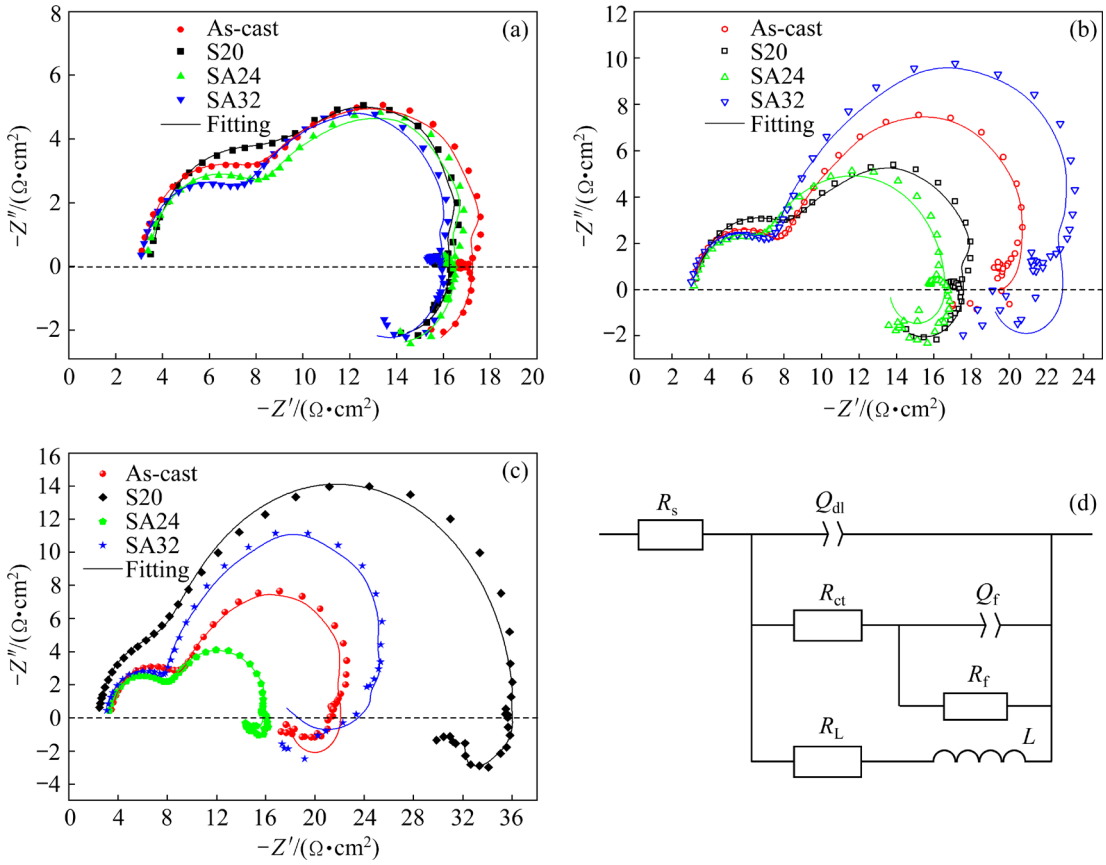

Fig. 12 Nyquist plots of composites with different states after immersion in 3 wt.% KCl solution for different time at ambient temperature and corresponding equivalent circuit: (a) 5 min; (b) 2 h; (c) 8 h; (d) Equivalent circuit

Table 2 Fitting parameters of EIS obtained from equivalent circuit in Fig. 12

Time	Sample	R_s/ ($\Omega\cdot cm^2$)	R_{ct}/ ($\Omega\cdot cm^2$)	Q_{dl}/ ($\Omega^{-1}\cdot cm^{-2}\cdot S^n$)	n_1	R_f/ ($\Omega\cdot cm^2$)	Q_f/ ($\Omega^{-1}\cdot cm^{-2}\cdot S^n$)	n_2	L/ ($H\cdot cm^{-2}$)	R_L/ ($\Omega\cdot cm^2$)	Chi-square
5 min	As−cast	3.37	6.06	1.65×10^{-6}	0.95	7.77	1.69×10^{-5}	0.97	9.69	31.12	2.74×10^{-4}
	S20	3.56	7.41	1.73×10^{-6}	0.94	7.60	1.45×10^{-5}	0.95	11.91	22.74	5.82×10^{-4}
	SA24	3.42	5.77	1.68×10^{-6}	0.97	7.30	2.13×10^{-5}	0.98	16.08	23.86	3.60×10^{-4}
	SA32	3.15	4.94	1.89×10^{-6}	0.95	7.59	2.34×10^{-5}	0.96	14.22	26.82	1.86×10^{-4}
2 h	As−cast	3.20	5.10	2.08×10^{-6}	0.94	13.25	4.18×10^{-5}	0.97	22.66	41.45	4.03×10^{-4}
	S20	3.32	6.03	1.96×10^{-6}	0.95	8.18	2.08×10^{-5}	0.94	15.27	27.68	2.61×10^{-4}
	SA24	3.27	4.76	2.37×10^{-6}	0.95	8.25	2.45×10^{-5}	0.97	21.62	46.61	1.86×10^{-4}
	SA32	3.09	4.34	2.51×10^{-6}	0.96	16.95	3.70×10^{-5}	0.98	20.41	33.58	5.68×10^{-4}
8 h	As−cast	3.53	6.63	2.61×10^{-6}	0.96	14.62	3.98×10^{-5}	0.94	19.39	52.58	2.45×10^{-4}
	S20	3.28	9.50	2.20×10^{-6}	0.95	25.53	8.78×10^{-6}	0.93	27.50	37.09	2.48×10^{-4}
	SA24	3.34	4.92	2.84×10^{-6}	0.97	7.73	2.53×10^{-5}	0.95	55.74	75.41	3.26×10^{-4}
	SA32	3.16	5.86	2.29×10^{-6}	0.96	18.64	3.47×10^{-5}	0.94	13.10	39.40	4.68×10^{-4}

the corrosion product, corresponding to the medium-frequency capacitance loop. L and R_L were connected in parallel with the medium-frequency capacitive loop, describing the ions exchange on the electrode surface [23], and R_s was solution resistance. A constant phase element Q was used instead of the pure capacitance due to the non-uniformity of the surface reaction. The value of n was a dispersion coefficient to reflect the deviation degree between Q and the ideal capacitance. The values n=1 and n=0 indicated that Q was a pure capacitor or resistor, respectively.

It was reported that the values of R_{ct} and R_f separately reveal the self-corrosion resistance of the electrode and the compactness of the corrosion product layer [24]. Figure 12(a) displayed the EIS of the composites obtained after immersion in 3 wt.% KCl solution for 5 min. The existence of medium-frequency capacitance loops and inductive loops indicated that the corrosion occurred immediately as soon as the composites were immersed in KCl solution. Table 2 shows that R_f values of all composites were generally low due to the less corrosion product. R_{ct} values increased in the following order SA32 < SA24 < as-cast < S20. Lower R_{ct} meant higher corrosion rates, the present result was consistent with the variation of the hydrogen evolution rates in the initial immersion stage. Besides, the Q_{dl} values of all composites displayed no significant difference, suggesting that they had similar electric double-layer structure at the beginning of immersion. With increasing immersion time (2 h), R_{ct} values of all composites were decreased in various degrees. This could be attributed to the damage in the original surface and the exposure of more cathodic phases, which resulted in the easier charge transfer of the electrode/solution interface. The decrease of R_{ct} consisted with the increased tendency of the corrosion rate with immersion time. Meanwhile, due to the increase of corrosion area, Q_{dl} values of all composites also rose, as shown in Table 2. Moreover, it can be observed that R_f and Q_f values of as-cast and SA32 composites were increased sharply, indicating that the corrosion product was gradually accumulated on their surfaces. While the increase in R_f values of S20 and SA24 composites was relatively small, there was less corrosion product on the surface of S20 and SA24 composites, due to the low corrosion rate and the instant exfoliation of the corrosion product respectively.

When the immersion time further increased to 8 h, the corrosion of all composites changed from local corrosion to overall corrosion. As discussed in the above section, the skeleton-like cathodic phases led to the formation of thick corrosion product layer on the surface of the as-cast and SA32 composites, which could act as a barrier to hinder the migration of the charges and ions. Therefore, the R_t and R_f values of the as-cast and SA32 composites were larger in the overall corrosion stage. In this stage, both the R_t and R_f values increased in the following

order SA24 < as-cast < SA32 < S20 (Table 2). It was noted that the S20 composites exhibited the largest R_t and R_f values. This was because a more stable and compact corrosion product layer could be formed on the S20 composites surface due to the dissolution of more Al in the Mg lattice. The experimental fact that the Al element could increase the stability of corrosion product film had been supported by many literatures [7,26,27]. The small Q_f value of the S20 composites could also prove that the corrosion product layer was more compact, while Q_f values of the as-cast and SA32 composites were larger due to the relatively porous corrosion product layer. Furthermore, it can be found that R_f and Q_f values of the SA24 composites did not significantly vary with immersion time, indicating that there was less corrosion product on the surface. While the smaller R_t of SA24 composites suggested which possessed lower corrosion resistance, thereby SA24 composites exhibited the highest corrosion rate. EIS results were in accordance with the immersion and polarization tests.

4 Conclusions

(1) The as-cast composites consisted of equiaxed α-Mg matrix, continuous β-$Mg_{17}Al_{12}$, τ-$Mg_{32}(Al,Zn)_{49}$, fishbone-like eutectic S-Al_2CuMg, and polygonal Mg_2Si phases. Solution treatment caused the β phase and τ phase to dissolve into the α-Mg matrix, the coarse eutectic S to become irregular block. And the polygonal Mg_2Si particles gradually spheroidized with the increasing solution treatment time increasing. The aging process after solution treatment could result in the precipitation of the β phase along the grain boundaries, while the blocky S phase did not change remarkably during the aging.

(2) The solution treatment greatly increased the ductility of the composites and slightly improved the ultimate compressive strength (UCS), but decreased the hardness. The aging treatment significantly increased UCS and hardness but only slightly decreased the ductility. After solution and aging treatment (420 °C, 20 h + 200 °C, 24 h), UCS, hardness and fracture strain of the composites reached 435 MPa, HB 124 and 8.3%, respectively, which was 29.8%, 18.1% and 36.1% greater than that of the as-cast composites.

(3) The degradation rate of the composites was primarily determined by the amount and distribution of the β phase. Solution treatment led to a decreased degradation rate because the cathodic β phase decreased. The aging process were favor of improving the degradation rate due to the precipitation of the β phase that could accelerate the micro-galvanic corrosion of the α-Mg matrix. However, once the aging time exceeded 32 h, the excessively precipitated β phase formed continuous network along the α-Mg grain boundary, which would act as a corrosion barrier to decrease the degradation rate of the composites. After solution treated at 420 °C for 20 h and aged at 200 °C for 24 h, the composites obtained outstanding overall performance, making it more beneficial to the applications as degradable downhole tools.

Acknowledgments

The present research was financially supported by the Natural Science Foundation of Shandong Province of China (No. ZR2019MEM020).

References

[1] MA Kai, LIU Shi-jie, DAI Chao-neng, LIU Xiu-ying, REN Jie, PAN Yuan-liang, PENG Yin-hong, SU Chen, WANG Jing-feng, PAN Fu-sheng. Effect of Ni on the microstructure, mechanical properties and corrosion behavior of $MgGd_1Ni_x$ alloys for fracturing ball applications [J]. Journal of Materials Science and Technology, 2021, 91: 121−133.

[2] LIU Lin, YU Si-rong, LIU En-yang, ZHAO Yan, WANG Bing-ying, NIU Ya-feng. Effect of Ni addition on the mechanical and degradation properties of hollow glass microsphere/Mg alloy composites [J]. Journal of Alloys and Compounds, 2021, 853: 157125.

[3] GENG Zhen-wei, XIAO Dai-hong, CHEN Liang. Microstructure, mechanical properties, and corrosion behavior of degradable Mg−Al−Cu−Zn−Gd alloys [J]. Journal of Alloys and Compounds, 2016, 686: 145−152.

[4] ZHAO Kai-kai, STEAD D, KANG Hong-pu, GAO Fu-qiang, DONATI D. Three-dimensional numerical investigation of the interaction between multiple hydraulic fractures in horizontal wells [J]. Engineering Fracture Mechanics, 2021, 246: 107620.

[5] LIU Kui, TALEGHANI A D, GAO De-li. Calculation of hydraulic fracture induced stress and corresponding fault slippage in shale formation [J]. Fuel, 2019, 254: 115525.

[6] ZHANG Cheng, WU Liang, HUANG Guang-sheng, CHEN Lin, XIA Da-biao, JIANG Bin, ATRENS A, PAN Fu-sheng. Effects of Fe concentration on microstructure and corrosion

of Mg−6Al−1Zn−*x*Fe alloys for fracturing balls applications [J]. Journal of Materials Science and Technology, 2019, 35: 2086−2098.

[7] WANG X W, WANG W, CHEN W, CHEN D M. Effect of Al addition and heat treatment on the microstructures and corrosion resistance of Mg−Cu alloys [J]. Journal of Materials Science and Technology, 2022, 98: 219−232.

[8] CHENG Peng, ZHAO Yu-hong, LU Ruo-peng, HOU Hua. Effect of the morphology of long-period stacking ordered phase on mechanical properties and corrosion behavior of cast Mg−Zn−Y−Ti alloy [J]. Journal of Alloys and Compounds, 2018, 764: 226−238.

[9] SRINIVASAN A, HUANG Y, MENDIS C L, BLAWERT C, KAINER K U, HORT N. Investigations on microstructures, mechanical and corrosion properties of Mg−Gd−Zn alloys [J]. Materials Science and Engineering A, 2014, 595: 224−234.

[10] WU Xia, PAN Fu-sheng, CHENG Ren-ju, LUO Shu-qing. Effect of morphology of long period stacking ordered phase on mechanical properties of Mg−10Gd−1Zn−0.5Zr magnesium alloy [J]. Materials Science and Engineering A, 2018, 726: 64−68.

[11] LIU Lin, YU Si-rong, LIU En-yang, ZHU Guang, LI Quan, XIONG Wei, WANG Bing-ying, YANG Xi-zhen. Enhanced mechanical and degradation properties of hollow glass microspheres/Mg matrix composites by incorporating copper power for degradable downhole tool applications [J]. Advanced Engineering Materials, 2021, 23: 2100615.

[12] NIU Hao-yi, DENG Kun-kun, NIE Kai-bo, CAO Fang-fang, ZHANG Xuan-chang, LI Wei-guo. Microstructure, mechanical properties and corrosion properties of Mg−4Zn−*x*Ni alloys for degradable fracturing ball applications [J]. Journal of Alloys and Compounds, 2019, 787: 1290−1300.

[13] CHANG Li-li, GUO Jing, SU Xiao-jing. Effect of Y on microstructure evolution and mechanical properties of Mg−4Li−3Al alloys [J]. Transactions of Nonferrous Metals Society of China, 2021, 31: 3691−3702.

[14] XIE Jin-shu, ZHANG Jing-huai, YOU Zi-hao, LIU Shu-juan, GUAN Kai, WU Rui-zhi, WANG Jun, FENG Jing. Towards developing Mg alloys with simultaneously improved strength and corrosion resistance via RE alloying [J]. Journal of Magnesium and Alloys, 2021, 9: 41−56.

[15] SONG Yan, YANG Hua-bao, CHAI Yan-fu, WANG Qing-hang, JIANG Bin, WU Liang, ZUO Qin, HUANG Guang-sheng, PAN Fu-sheng, ATRENS A. Corrosion and discharge behavior of Mg−*x*La alloys (*x*=0.0−0.8) as anode materials [J]. Transactions of Nonferrous Metals Society of China, 2021, 31: 1979−1992.

[16] CHEN L, WU Z, XIAO D H, GENG Z W, ZHOU P F. Effects of copper on the microstructure and properties of Mg−17Al−3Zn alloys [J]. Materials and Corrosion, 2015, 66: 1159−1168.

[17] XIAO D H, GENG Z W, CHEN L, WU Z, DIAO H Y, SONG M, ZHOU P F. Effects of alloying elements on microstructure and properties of magnesium alloys for tripling ball [J]. Metallurgical and Materials Transactions A, 2015, 46: 4793−4803.

[18] LIU Lin, YU Si-rong, NIU Ya-feng, LIU En-yang. Preparation and properties of hollow glass microspheres reinforced Mg alloy degradable composites [J]. Journal of Alloys and Compounds, 2020, 835: 155198.

[19] LIU Lin, YU Si-rong, LIU En-yang, ZHAO Yan, WANG Bing-ying, NIU Ya-feng, BI Xiao-jian, ZHU Guang, LI Quan. Investigations on the microstructure and degradation behavior of hollow glass microspheres/Mg alloy composites [J]. Advanced Engineering Materials, 2021, 23: 2001301.

[20] LUO Sheng-min, WU Yong-kang, Li Yu-cheng, WANG Dong-fang, KIM D, SONG Jin-liang, ZHANG Guo-ping. Nanoindentation-enhanced screening of hydraulic fracturing fluid additives [J]. International Journal of Coal Geology, 2021, 240: 103744.

[21] SONG G L, ATRENS A. Corrosion mechanisms of magnesium alloys [J]. Advanced Engineering Materials, 1999, 1: 11−33.

[22] XIE Jin-shu, ZHANG Jing-huai, ZHANG Zhi, YANG Qiang, GUAN Kai, HE Yu-ying, WANG Ru, ZHANG Hao, QIU Xin, WU Rui-zhi. New insights on the different corrosion mechanisms of Mg alloys with solute-enriched stacking faults or long period stacking ordered phase [J]. Corrosion Science, 2022, 198: 110163.

[23] CHEN Xing-rui, WANG He-nan, ZOU Qi, LE Qi-chi, WEN Cui-e, ATRENS A. The influence of heat treatment on discharge and electrochemical properties of Mg−Gd−Zn magnesium anode with long period stacking ordered structure for Mg-air battery [J]. Electrochimica Acta, 2021, 367: 137518.

[24] YAN Xu-dong, WAN Peng, TAN Li-li, ZHAO Ming-chun, SHUAI Ci-jun, YANG Ke. Influence of hybrid extrusion and solution treatment on the microstructure and degradation behavior of Mg−0.1Cu alloy [J]. Materials Science and Engineering B, 2018, 229: 105−117.

[25] ARRABAL R, PARDO A, MERINO M C, MOHEDANO M, CASAJÚS P, PAUCAR K, GARCÉS G. Effect of Nd on the corrosion behaviour of AM50 and AZ91D magnesium alloys in 3.5 wt.% NaCl solution [J]. Corrosion Science, 2012, 55(2): 301−312.

[26] ESMAILY M, BLÜCHER D B, SVENSSON J E, HALVARSSON M, JOHANSSON L G. New insights into the corrosion of magnesium alloys—The role of aluminum [J]. Scripta Materialia, 2016, 115: 91−95.

[27] JEURGENS L P H, VINODH M S, MITTEMEIJER E J. Initial oxide-film growth on Mg-based MgAl alloys at room temperature [J]. Acta Materialia, 2008, 56(17): 4621−4634.

热处理对空心玻璃微球增强 Mg−15Al−5Zn−1.5Cu 复合材料力学性能和降解行为的影响

刘 林[1]，于思荣[1]，王炳英[1]，朱 光[2]，刘恩洋[1]

1. 中国石油大学(华东) 材料科学与工程学院，青岛 266580；
2. 洛阳船舶材料研究所 海洋腐蚀与防护重点实验室，青岛 266237

摘 要：通过热处理改善空心玻璃微球/镁合金(Mg−15Al−5Zn−1.5Cu)可溶复合材料的综合性能，采用金相显微镜和扫描电子显微镜等手段分析复合材料在热处理过程中的微观结构变化。通过压缩试验、浸泡试验和电化学测试等手段探究热处理条件对复合材料的力学性能和溶解行为的影响，并揭示其影响机理。结果表明，热处理主要通过影响 $Mg_{17}Al_{12}$ 相和 Al_2CuMg 相数量、形态和分布影响复合材料的力学性能和溶解速率；经 420 ℃固溶处理 20 h 和 200 ℃时效处理 24 h 后，复合材料的基体晶粒组织和析出相分布更加均匀，成分偏析和残余应力被消除。获得了优异的综合性能，极限抗压强度、布氏硬度和断裂应变分别可达 435 MPa、HB 124 和 8.3%，室温下在 3% KCl(质量分数)溶液中的平均溶解速率可达 151 mg/(cm^2·d)，更有利于该复合材料在可溶井下工具中的应用。

关键词：可溶镁基复合材料；热处理；显微组织；力学性能；溶解行为

(Edited by Xiang-qun LI)